macQsimal	Title	Deliverable Number
	Low-density OPM demonstrator and benchmarking report	**D4.5**
Project Number **820393**		Version **1**

H2020-FETFLAG-2018-2021

macQsimal

Miniature Atomic vapor-Cell Quantum devices for SensIng and Metrology AppLications

Deliverable D4.5

Low-density OPM demonstrator and benchmarking report

WP4 – Miniature optically-pumped magnetometers

Authors: Michael Zugenmaier (UCPH), Hans Stærkind (UCPH), Jeppe Detlefsen (UCPH), Eugene Polzik (UCPH)

Lead participant: UCPH

Delivery date: 30.04.2020

Dissemination level: Public

Type: R (Document, Report)

macQsimal	Title	Deliverable Number
		D4.5
Project Number	**Low-density OPM demonstrator and benchmarking report**	Version
820393		**1**

Revision History

Author Name, Partner short name	Description	Date
Michael Zugenmaier (UCPH)	Draft deliverable	19.04.2021
Christoph Affolderbach (UNINE)	Review	27.04.2021
Michael Zugenmaier (UCPH)	Final Version	29.04.2021
Johannes Ripperger (accelCH)	Final checks and layout	03.05.2021

Abbreviations

MCG	Magnetocardiography
MIT	Magnetic induction tomography
MORS	Magneto-optical resonance spectroscopy
MRI	Magnetic resonance imaging
OPM	Optically-pumped magnetometer
RF	Radio-frequency
SNR	Signal-to-noise ratio
WP	Work Package

Partner short names

accelCH	accelopment Schweiz AG
CSEM	CSEM SA – Centre Suisse d'Électronique et de Microtechnique, CH
UCPH	Københavns Universitet, DK (NBI – Niels Bohr Institut)
UNINE	Université de Neuchâtel, CH

macQsimal	Title	Deliverable Number
	Low-density OPM demonstrator and benchmarking report	**D4.5**
Project Number **820393**		Version **1**

Contents

Executive Summary

This deliverable report summarizes the characterization and benchmarking results achieved to-date for the low-density OPM within macQsimal WP4. The report is encompassing the results within the following items within task T4.2

1. Validation of cell performance (T4.2.1)
2. Demonstration of a miniaturized fibre-coupled OPM sensor reaching 10s of fT for detection of both low frequency (DC- few 100 Hz) and high frequency (kHz, MHz) magnetic fields (T4.2.2). Discussion of using this sensor to repeat and improve MCG measurements (T4.2.3)
3. Development of techniques for imaging electrical conductivity with OPMs with measurements on high conductivity samples (metals) and low conductivity phantoms (salt-water). (T4.2.4)
4. (T4.2.5) Development and testing of strong field OPM array for improving high field (> 1 Tesla) MRI image quality. Target sensitivity of a few tens of nT/√Hz.

Need for the Deliverable

This report summarizes the required benchmarks and tests for the individual implementations of the low-density OPMs.

Objectives of the Deliverable

With the help of this deliverable, we summarize the achievements up to date and outline future steps.

Outcomes

We have demonstrated low-density OPMs using glass-blown vapour cells. We have tested and benchmarked a fibre-coupled OPM sensor with 200fT/sqrt(Hz) sensitivity at low magnetic fields (75 fT/sqrt(Hz) for RF magnetic field sensing). This sensor would allow to repeat MCG measurements that have been previously demonstrated with a similar free-space setup. We have developed techniques for imaging of electrical conductivities that allowed the first contact-less measurement of few mL volumes of near-Siemens-per-meter conductivity salt-water phantoms. We have developed an array of OPMs suitable for field measurements within an MRI scanner and demonstrated its capability by measurement of the diamagnetic shift of caesium with unprecedented precision.

Next steps

Further improvement of the electrical conductivity imaging – reaching SNR to apply it to biological samples, envisioning 3D imaging. Evaluating the possibility to use quantum enhanced measurement (spin squeezing) towards the improvement of sensitivity.

Further noise-investigation and testing fibre-coupled OPM sensor in application.

Application of the array of strong field OPMs for MRI image improvement.

1   Low-density OPM introduction

The sensitivity of OPMs is fundamentally related to the number density of the vapor and by the atomic spin coherence time. The density can be increased by increasing the temperature. However, the atomic collisions due to a high density can lead to atomic line shifts and they can decrease the coherence time. High temperature can prohibit the use of anti-relaxation coating that boosts the coherence time. High temperatures can also increase the required stand-off distance required between an OPM and a heat-sensitive sample. We are here investigating low-density OPMs. Their densities are below the regime where the above complications come into play, resulting in working temperatures of about room temperature up to 50°C.

We use two distinct working principles for the low-density OPMs. The first is Faraday rotation, which is off-resonant detection of the atomic spin precession. This is used for the low-field OPM demonstrators from DC to MHz frequencies. The second is on-resonant absorption, which is used in the strong field OPM sensor.

1.1   Faraday rotation sensing

The Faraday effect is exploited in our low-field OPM sensors. Optical pumping is used to generate atomic spin polarization, which precesses due to an external magnetic field and is detected optically, by Faraday rotation of an off-resonant probe beam. The Faraday interaction rotates the angle of the linear input polarization of the probe light by an amount proportional to the projection of the atomic spin in the probe propagation direction. Analysing the rotation angle with balanced polarimetry allows us to determine the spin projection.

We can apply a known static magnetic field. Then, the precession frequency of the atomic spin is proportional to the strength of the magnetic field, with the known atomic gyromagnetic ratio as proportionality constant. Changing the strength of the static magnetic field we can thus tune the resonance frequency where the OPM sensitivity is optimal, from DC to MHz.

The cell walls are coated with paraffin-like anti-relaxation coatings. These enable the atoms to experience many wall collisions with no change of their spin state. This extension of the coherence time boosts the sensitivity of the OPM.

1.2   Absorption sensing

For absorption sensing in the strong-field OPM sensors, we arrange an on-resonant pump beam and a probe beam passing counter-propagating through an atomic vapour cell. In this setup the probe can experience a Doppler-free absorption profile of the optical transition. Frequency modulation of the beam allows to derive a dispersive signal centred on the optical transition. If the atomic vapour experiences a magnetic field, the optical transition and thus the dispersive signal shifts. Measurement of the frequency shift directly yields the magnetic field strength.

The vapour cells only contain caesium to avoid line broadening that would otherwise arise from collisions with an eventual buffer gas background.

2   Cell performance validation

The low-density OPMs utilize cells that contain caesium and possibly also a paraffin coating. The cells do not contain any buffer gas, therefore the current method of our partner CSEM to produce chip style cells is not directly applicable and we have instead used glass-blown cells.

2.1   Paraffin-coated cells

We chose a cell geometry of a cubic cell with approximately 5 mm side length. This was a good compromise between number of atoms and thus possible sensitivity and spatial resolution. Since we had worked with similar cells before, we also had a working process for how to produce these cells with glass-blowing and had a few backup cells fabricated by a glass-blower.

For the standard fabrication of these cells, we use pre-fabricated glass tubes. Although on one hand this simplifies the fabrication process, it also results in the disadvantage that the sides of optical access for both probing and pumping beams do not carry antireflection coatings and only have modest surface quality given by the pre-fabricated glass tubes. We therefore investigated a different procedure for glass-blown cells, using optical quality windows for the probe beam direction. The advantages would have been

- Bigger possible filling of the cross section with the probe beam due to less beam distortion at the rims. This in turn would decrease broadband noise that ultimately could limit sensitivity.
- High probe transmission (possible with AR-coated windows) would facilitate multipass/cavity setups yielding better sensitivity. Furthermore, they could simplify gradiometer setups and quantum back-action noise evading measurements, ultimately improving quantum-noise limited magnetometer performance.

2.1.1   Cell transmission

In collaboration with a local glass-blower, we fabricated ~5 mm cubic cells with uncoated, optical-quality glass windows.

Figure 1. Glass-blown cells with 5mm x 5mm square cross section and optical windows.

We tested the optical quality of the fabricated cells by observing a grid through the cell under a microscope. We can clearly see the improvement in the observed distortion in Figure 2. Whereas in the backup cell, only the centre 3 mm appear undistorted, in the cell with window, there is only marginal distortion when approaching the rim. The fabrication method gave reliably similar results for all tested cells.
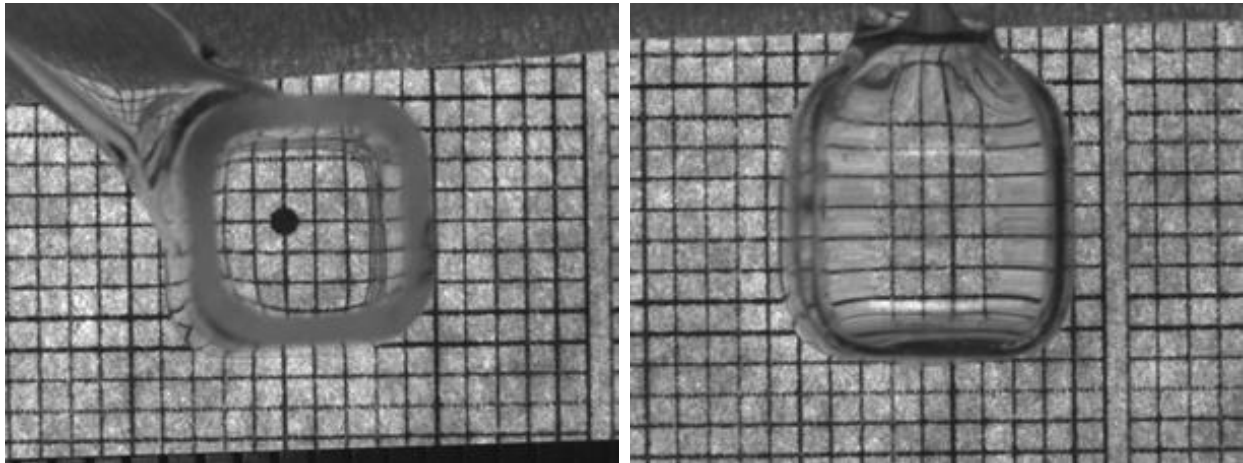

Figure 2. Optical quality assessment: (left) Example of transmission through a cell with window (Nc5). Grid spacing 0.8mm. (right) Comparison to backup cell, cubic 5mm (cubicA3). The image distortion is strongly reduced for the new Nc5 cell.

The next steps were to fill the empty cells with paraffin and caesium. Here we realised, that the fabricated cells appeared not to be vacuum-tight and could therefore not be filled. A possible explanation is that great care was taken to not heat the windows excessively during the glass-blowing procedure to prevent deformation. On the other hand, this appeared to have left a leaky connection between the glass parts. The backup cells with 5mm cubic dimension were vacuum-tight. These were filled with caesium (no buffer gas) and the inside walls were coated with paraffin anti-relaxation coating.

The fabrication of good optical-quality, vacuum-tight miniature cells will have to be investigated further. However, we emphasize that for the current noise performance of the OPMs, the backup cells' performances are sufficient.

2.1.2 Coherence time

We have tested the coherence time of the backup cells using magneto-optical resonance spectroscopy (MORS) [Julsgaard03]. We optically pump the atomic spins with circularly polarized pump and repump light that is aligned with the bias magnetic field. After turning off the pump light we apply a few cycles of an oscillating magnetic field perpendicular to the bias magnetic field. The oscillation frequency is chosen resonant with the Larmor frequency such that the atomic ensemble spin is excited out of its steady state. After turning the oscillating field off, the ensemble spin precesses around the bias magnetic field. Decoherence of the atomic spins leads to the decrease of the ensemble spin component transverse to the magnetic field with the characteristic coherence time T_2. Weak off-resonant linearly polarized probe light is transmitted through the vapour cell in the direction transverse to the magnetic field. Faraday interaction causes the light polarization to rotate proportional to the spin component along the probe propagation direction. Measuring this polarization rotation in a balanced fashion allows to directly observe the decoherence time T_2 as the characteristic time of the exponentially decreasing envelope of the oscillating signal. The measured coherence times are in the range of 20 ms and thus on par with paraffin-coated cells of similar dimensions. An example is shown in Figure 3.
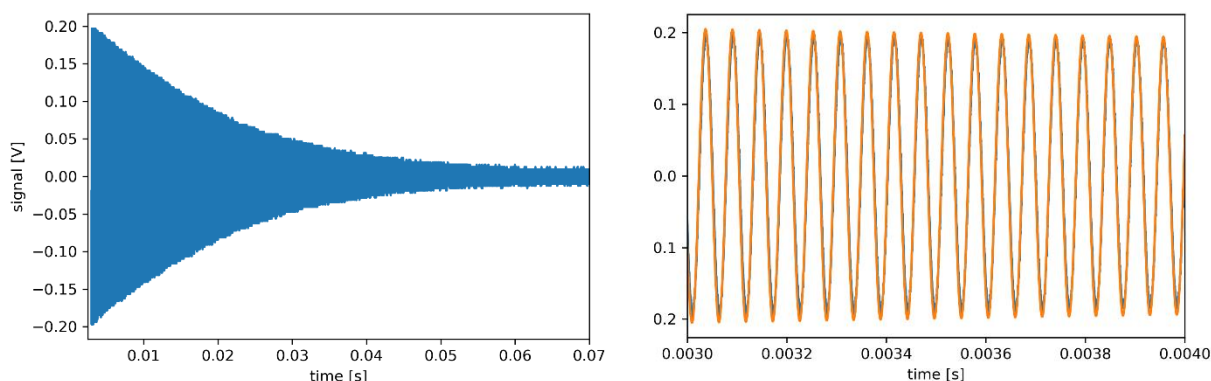
Figure 3. Pulsed MORS measurement, balanced detector signal after pumping and short excitation pulse. (left) shows the full data (blue) with decaying envelope yielding $T_2 = 17$ ms. (right) shows cut out from (left), with the fit (yellow) added on top. The oscillating data (blue) agrees well with the fit and is barely visible behind the yellow line.

2.2 Commercial caesium only cells

Six cells have been produced by Precision Glass Blowing with good vacuum tightness, containing caesium only (no buffer gas, no wall coatings). One for the reference sensor head outside the MRI scanner, four for the probe sensor heads inside the MRI scanner, and one spare. Pressure is set by the natural caesium vapor pressure. Transmission is on the order of 96 % and (total) reflection is about 2 %. The cell outer diameter is 6 mm, and the optical path length is 5 mm (they cannot make this smaller). The stem is about 12 mm long (they can make this as small as 3 mm).

By 1.2 W of optical heating at 805nm the density can be increased to about 35e16 m^{-3}:

This corresponds to about 46 °C. That is with the current strong field OPM probe sensor head design, inside the MRI scanner. Heating with more than 1.2 W will make the sensor head expand thermally, so that fibre-coupling is lost. It is worth noticing that it takes about an hour for the system to reach an equilibrium. And that the dynamics shown in Figure 4 depend strongly on how long the cell has not been in use:

- Red line: 3 months
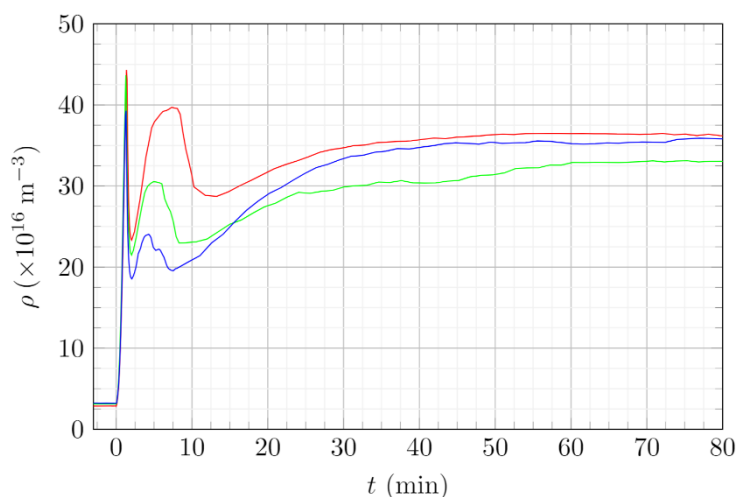- Green line: 1 week
- Blue line: 1 day

Figure 4. Density evolution for different cells when turning on heating.

It is understood that the density corresponds to the coldest point in the cell; that is the bottom of the stem, pointing away from the heating laser beam. Using a cell with a shorter stem should enable higher densities, with the same or lower heating power.

macQsimal	Title	Deliverable Number
	Low-density OPM demonstrator and	**D4.5**
Project Number	**benchmarking report**	Version
820393		**1**

The signal strength from the reference sensor head and the probe sensor head is measured as a function of temperature, and probing power:
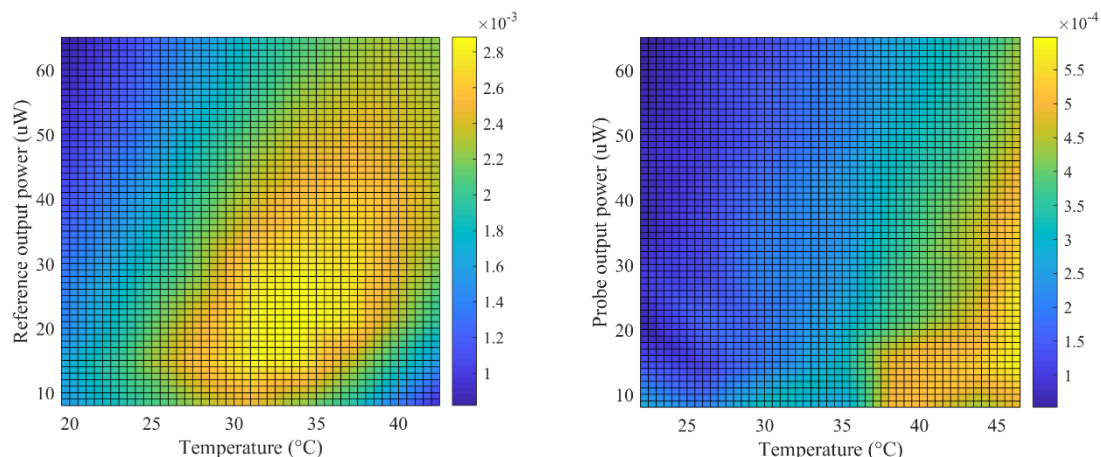

Figure 5. Signal strength for reference sensor head (left) and probe sensor head (right) setup measured for different temperatures and laser powers. The signal strength is here defined as the second derivative of the normalized transmission profile, at the peak. Thus, it has units of 1/MHz^2.

It is seen that there is no need for higher temperature for the reference, but the probe sensitivity would benefit from higher temperatures – that is shorter stem. This can easily be achieved by Precision Glass Blowing. What they however cannot produce is a small cell in terms of optical path length. If we want to increase the spatial resolution of our magnetometer, this will probably have to be realized with chip-style cells. For all our proof-of-concept work, this is however not very important. Also, to lower the cost, it would be nice to implement chip-style cells. We hope that high vacuum chip-cells without buffer gas will be available when this becomes relevant to us.

3 Fibre-coupled OPM sensor

In this section we describe the efforts in the tasks 4.2.2 and 4.2.3, namely the laboratory demonstration of high sensitivity magnetometer with anti-relaxation coated vapor cells, aiming to reach the 10's of fT/sqrt(Hz) range for low and high frequencies and the implications for the development of magnetocardiography.

We designed a compact optically-pumped magnetometer shown in Figure 6. A small form factor of 10 x 6 x 1.5 cm makes the sensor head very versatile. Furthermore, short optical pathlengths avoid susceptibility to mechanical vibrations that were the main noise source in the magnetocardiography application setup that we have already investigated in the preparation for macQsimal [Jensen18]. Fibre-coupling the sensor head allows us to use high quality table-top laser systems. We used the design experience with the strong field OPM, leading to a similar 3d printing approach with a metal-free sensor head.
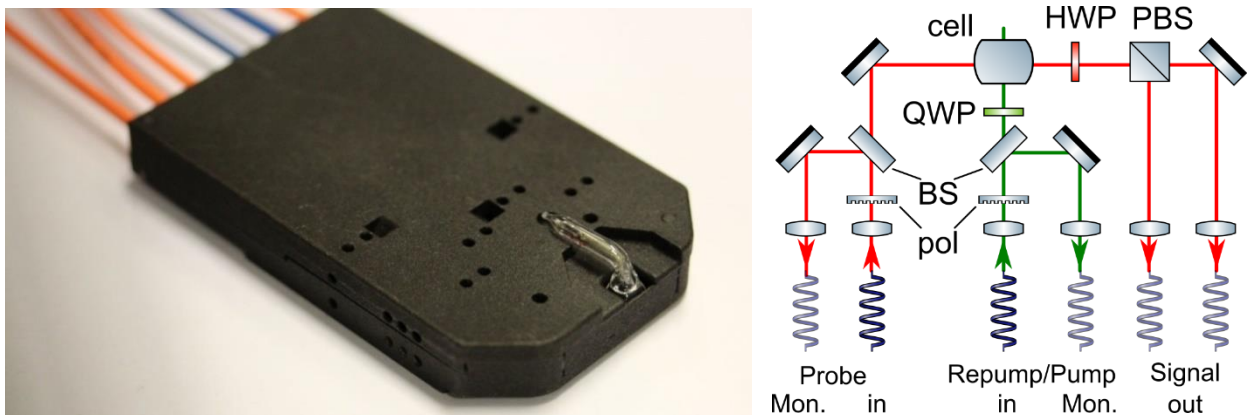

Figure 6. Left: Photograph of the assembled fibre-coupled sensor head. Right: Corresponding simplified schematics of the optics (BS: beam splitter, PBS: polarizing beam splitter, pol: polarizer, QWP: quarter-wave plate, HWP: half-wave plate, Mon: monitor output).

The optical design of the sensor is schematically shown in Figure 6 (right). It is similar to the setup in [Jensen18] and similar to the MIT setup shown in Figure 11(b) a two-beam setup. Circularly polarized repump and pump light aligns the atomic spins of caesium atoms in a 5 mm cubic vapor cell along a bias magnetic field. Linearly polarized probe light, detuned from resonance by 1.6 GHz is transmitted through the cell perpendicular to the pumping direction. Repump, pump and probe light are here supplied to the sensor head via single-mode fibres. The polarization rotation of the probe light due to the Faraday interaction is measured with a balanced polarimetry setup, where the polarizing beam splitter (PBS) is located in the sensor head. The two output ports of the PBS are coupled via multi-mode fibres to a balanced detector. Two more multi-mode fibres can be used to monitor the input powers.

The 3d printed assembly comes with the disadvantage of limited alignment possibilities compared to a table-top free space setup. However, good fibre coupling could be achieved with overall coupling losses below 5%.

We present in the following the tests of the fibre-coupled magnetometer for the detection of RF magnetic fields in the range of few 100 kHz and magnetic fields in the very low range below a few hundred Hz.

3.1 RF field measurements

The fibre-coupled sensor head is placed inside a magnetic shield to remove magnetic influence from the outside. Coils are added to prepare a homogeneous magnetic bias field of about 0.5 G along the pumping direction at the position of the cell. An additional Helmholtz coil pair can be used to apply an oscillating

macQsimal	Title	Deliverable Number
	Low-density OPM demonstrator and	**D4.5**
Project Number	**benchmarking report**	Version
820393		**1**

magnetic field perpendicular to pumping and probing. This RF field is the field that is to be detected by the OPM and is used for calibration.

We calibrate the magnetic RF field of the excitation by driving Rabi oscillations between Zeeman levels. The Rabi frequency allows us to directly determine the magnetic field strength. We then attenuate the magnetic RF field and record the magnetometer signal. Its power spectral density around the Larmor frequency is shown in Figure 7 in blue. Here we clearly see a peak at the excitation frequency. Comparing with the magnetometer noise floor recorded in the absence of an applied RF field shown in green we determine the sensitivity of the magnetometer where the signal-to-noise ratio would be unity to be 75 fT/sqrt(Hz) at 152 kHz Larmor frequency.
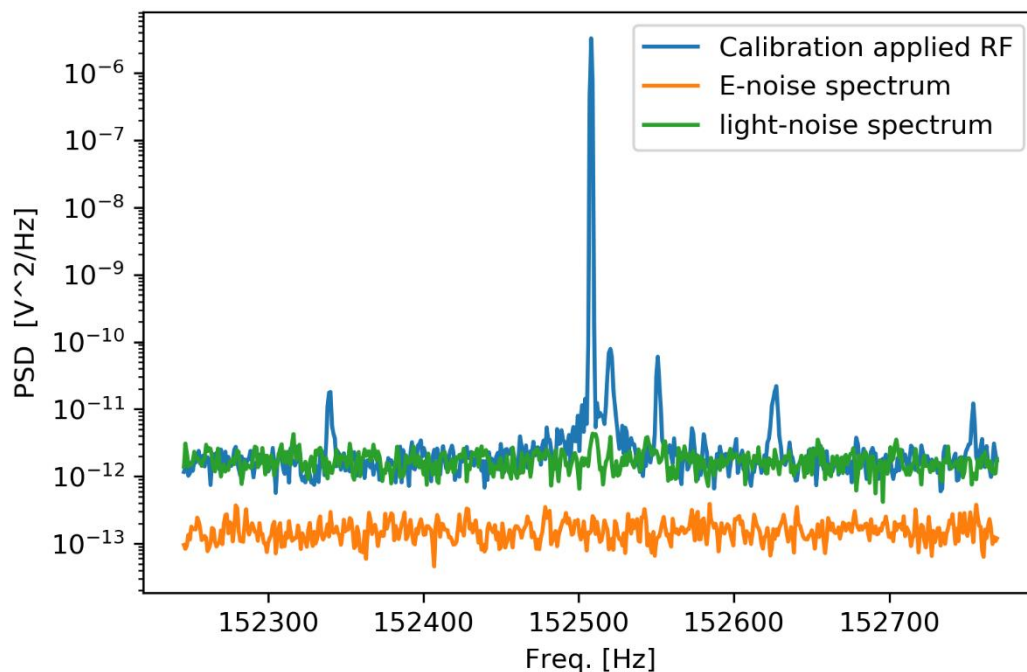

Figure 7. Power spectral density around the Larmor frequency. Calibration peak with applied RF magnetic field (blue), noise level without applied RF magnetic field (green) and electronic noise floor (yellow).

3.2 Low field measurements

The working principle described in the following is similar to [Jensen18]. The caesium atoms are described by their total angular momentum J. In the absence of a magnetic field this is pumped along the x-direction. For a fully pumped ensemble where all N_A atoms are in the $F = 4, m_F = 4$ state the total angular momentum is $J_{max} = 4N_A\hat{x}$. The time evolution of the total angular momentum can be modelled with the optical Bloch equation

$$\frac{dJ}{dt} = \gamma J \times B + \Gamma_p J_{max} - \left(\Gamma_p + \Gamma_{pr} + \Gamma_{dark}\right)J$$

with the gyromagnetic ratio γ, B the external magnetic field, Γ_p the rate of optical pumping, Γ_{dark} the decay rate in the absence of light and Γ_{pr} the decay rate due to the probe. If we assume that the magnetic field is varying on a timescale comparable to or faster than the coherence time of the cell, we find for the magnetometer signal

$$S(t) = c \int_{t'=-\infty}^{t'=t} e^{-\Gamma(t-t')} B_y(t')dt'$$

macQsimal	Title	Deliverable Number
	Low-density OPM demonstrator and	**D4.5**
Project Number	**benchmarking report**	Version
820393		**1**

With the normalization constant c. We identify this as a convolution of the magnetic field $B_y(t')$ with the magnetometer response (Kernel) function $K(t) = ce^{-\Gamma t}$. Therefore, the magnetic field can be obtained by deconvolution of the magnetometer signal with the Kernel function.

The sensor is placed inside a magnetic shield. We then zero the residual magnetic field with compensation coils. We determine the Kernel function in two steps. First, we apply an approximated impulse response, i.e. a 100 μs short square pulse of magnetic field along the y-direction. This is shown in Figure 8.
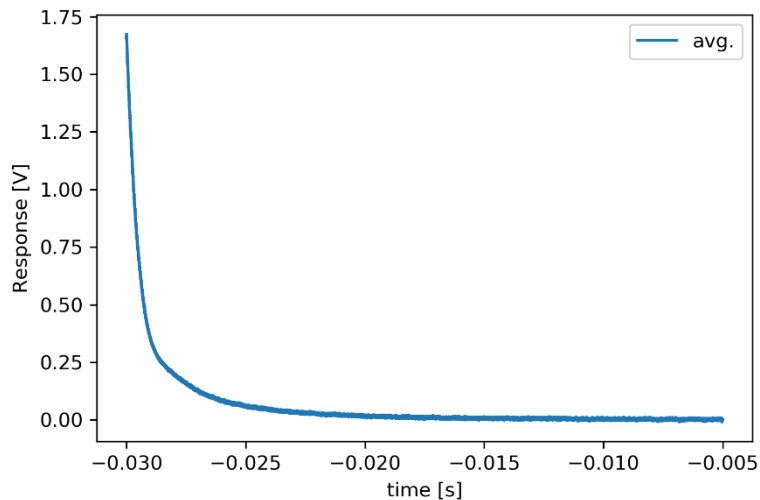

Figure 8. Measured Kernel function, average of 10 individual measurements.

Then, to determine the normalization constant we apply a single 100 Hz oscillation of a magnetic field of calibrated strength using an extra coil. The calibration of the strength has been done by observing the Larmor frequency shift when applying similar voltage in static conditions. We note that the we cut out the frequency contributions to the Kernel above 2 kHz to reduce the impact of high frequency noise present in the measured Kernel. The atomic bandwidth $1/(2\pi T_2)$ is about 50 Hz for the specific settings. However, the deconvolution procedure allows us to measure frequency components well above.

We show in Figure 9 the oscillation input and the signal calculated by deconvolution of the magnetometer signal with the measured Kernel function.
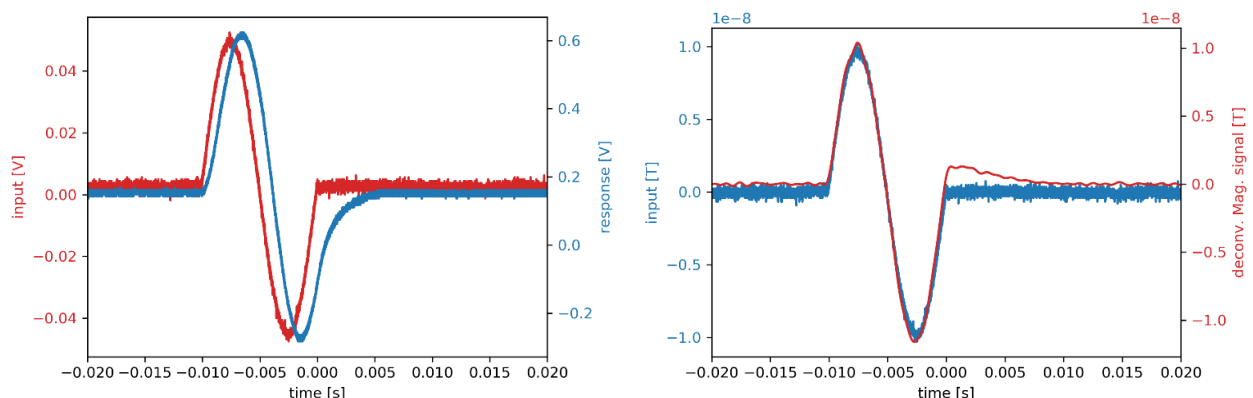

Figure 9. Left: 100 Hz single cycle voltage input (red) and resulting magnetometer signal (blue). Right: Magnetic field strength of single cycle input (blue) which equals the red line from the left figure calibrated to magnetic field units and deconvoluted magnetometer signal (red).

We measure the noise floor of the magnetometer while not applying any extra magnetic field. We deconvolve the magnetometer signal and obtain the root spectral density as shown in Figure 10. The

macQsimal	Title	Deliverable Number
	Low-density OPM demonstrator and	**D4.5**
Project Number	**benchmarking report**	Version
820393		**1**

resulting sensitivity is below 1pT/sqrt(Hz) in a range from approximately 3Hz to 1kHz except for increased noise around 50Hz. The sensitivity even reaches approximately 200 fT/sqrt(Hz) in a range from 5Hz to 200Hz, except for a few more noisy peaks. The origin of these noise peaks is currently still under investigation.
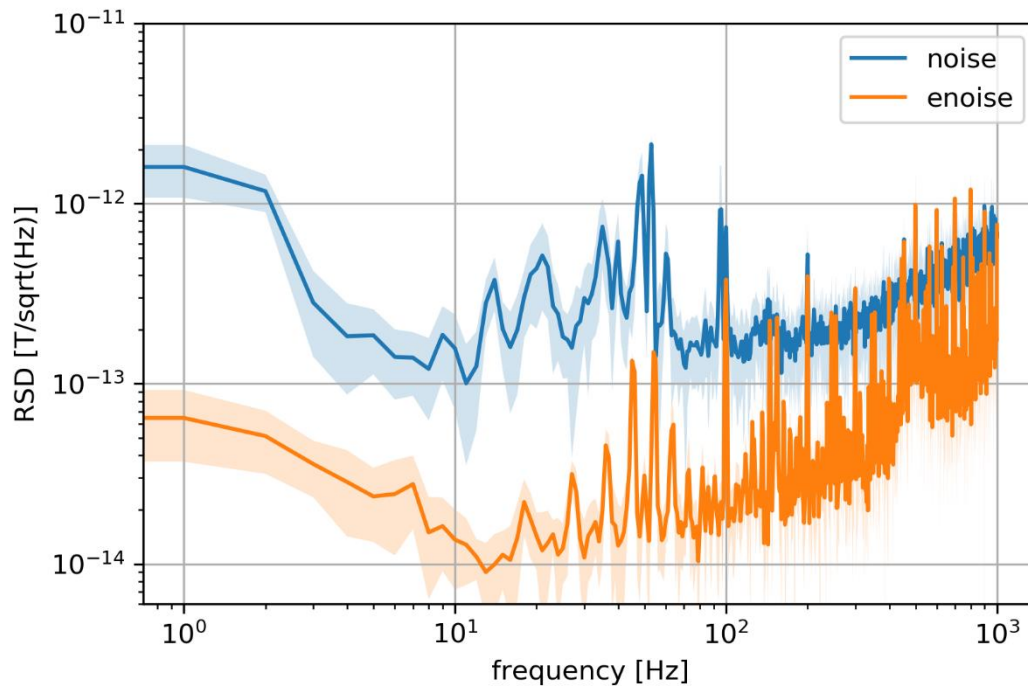

Figure 10. Low field magnetometer sensitivity. Square root of the power spectral density plotted versus frequency for the magnetometer signal (blue) and the electronic noise floor (yellow). The lines show the average of 10 measurements with the shaded area as standard deviation.

3.3 Discussion about application for MCG

During the preparation for macQsimal we have already developed MCG measurements with OPMs [Jensen18]. There, with a setup using free space optics, the heartbeat from isolated guinea pig hearts was measured. The sensitivity in those measurements were limited by mechanical vibrations to 120 fT/sqrt(Hz) in the 100-500 Hz range and 300 fT/sqrt(Hz) for the wider range 5-1000 Hz, not limited by the fundamental quantum spin-projection noise estimated to be around 8 fT/sqrt(Hz). We could demonstrate that the device was capable of measuring the cardiac electrographic intervals, such as the RR- and QT-interval, and detecting drug-induced prolongation of the QT-interval, which is important for medical diagnostics.

The OPM presented in this report is essentially the fibre-coupled 3D printed and miniaturized version of the free-space setup of [Jensen18]. The miniaturization should in principle make the setup less prone to mechanical vibrations. However, the observed sensitivity is about the same, marginally better around 10 Hz, marginally worse above 100Hz. The origin of the noise is currently under investigation. Possibly, the fibre-coupling approach, even though adding flexibility to the setup, introduces excess noise to the system.

To make new MCG measurements on guinea pig hearts a valuable scientific contribution requires the ability to make new innovative measurements, e.g. measurement at bigger distances than the 16 mm demonstrated in [Jensen18]. As the magnetic field drops with distance ($B \propto x^{-1.7}$ shown ibid.) a significant improvement in sensitivity will be necessary to measure at increased standoff distance.

4 Electrical conductivity mapping

Optical magnetometers can be used to image non-invasively the electrical conductivity of samples using a technique known as magnetic induction tomography (MIT). These samples under investigation can be e.g. metal samples or even organic tissue like a heart where the detection of regions of low conductivity can facilitate the diagnosis of heart arrythmia. One or more coils are used to induce eddy currents in the sample and an image can be reconstructed from the measurements of the magnetic field.

The coil 1 generates a primary magnetic field B_1 oscillating at the frequency ω. The generated eddy current in the sample in turn creates the magnetic field B_{ec}. The primary field is attenuated while penetrating into the sample with the characteristic length given by the skin depth.

4.1 Experimental Setup

Our experimental setup is shown in Figure 11 from the side (a) and from the top (b). The paraffin-coated vapour cell is centred between two coils. Above the primary coil 1, the sample with salt-water (or metal) can be mounted and moved. Optical pumping with circularly-polarized resonant repumping and pumping light (transitions shown in c) orients the atomic spins in the caesium vapour cell along the bias magnetic field $B_0\hat{x}$. This bias field defines the Larmor resonance frequency of the precessing atomic spins. We consider an oscillating magnetic field $\boldsymbol{B}_{rf} = B_c \cos(\omega t)\hat{\boldsymbol{y}}$ that we want to detect.

For the total angular momentum in the F=4 ground state manifold $\boldsymbol{J}$ we can model the time evolution using the Bloch equations

$$\frac{d\boldsymbol{J}}{dt} = \gamma \boldsymbol{J} \times \boldsymbol{B} + \Gamma_p \boldsymbol{J}_{max} - \left(\Gamma_p + \Gamma_{pr} + \Gamma_{dark}\right)\boldsymbol{J}$$

With the gyromagnetic ratio γ, $\boldsymbol{B} = B_0\hat{x} + \boldsymbol{B}_{rf}$, Γ_p the rate of optical pumping, Γ_{dark} the decay rate in the absence of light and Γ_{pr} the decay rate due to the probe. In the frame rotating with the Larmor frequency (denoted primed) this leads e.g. for the z-component to a Lorentzian response of the steady state solution

$$J_z'^{ss} \propto \frac{\gamma B_c \delta\omega/2}{\Delta^2 + (\delta\omega)^2 + \gamma^2 B_c^2/4}$$

Where $\delta\omega = \Gamma_p + \Gamma_{pr} + \Gamma_{dark}$ and $\Delta = \omega - \omega_L$ is the detuning from the Larmor frequency ω_L. The atoms are probed with linearly polarized probe light detuned by 1.6 GHz. Its polarization is rotated due to the Faraday effect by an amount proportional to the spin component along the probe propagation direction. The light polarization rotation is then measured with a balanced detection scheme leading to a magnetometer signal

$$S(t) \propto J_z(t) = \sin(\omega t)J_y'(t) + \cos(\omega t)J_z'(t)$$

Lock-in detection at the frequency ω provides the in-phase component X and the out-of-phase component Y.
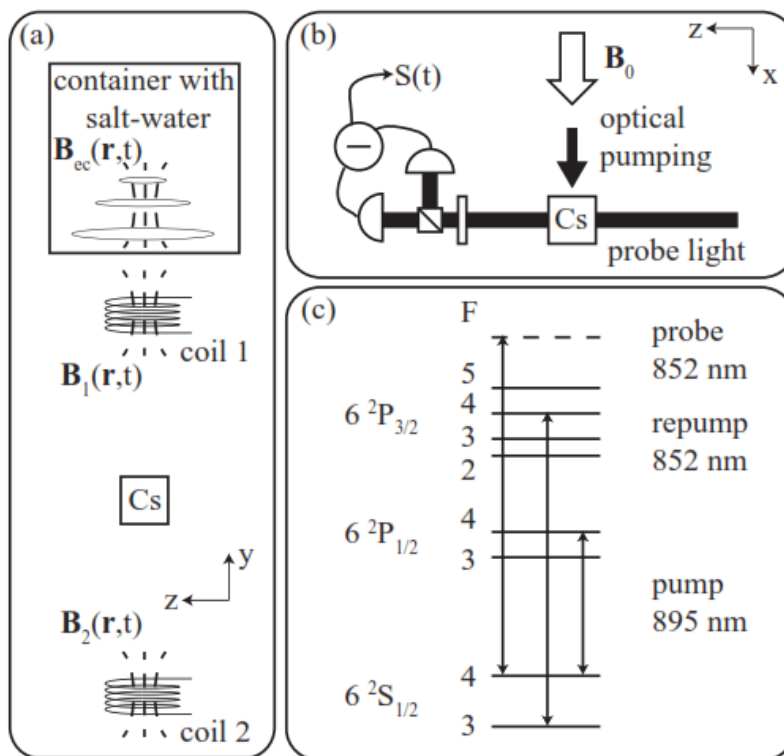
Figure 11. (a) Setup for detecting eddy currents. (b) Optical pumping and probing of the cesium atomic spins. (c) Caesium level scheme and laser wavelengths. The probe light is 1.6 GHz detuned. Figure from [Jensen19].

4.2 Metal measurement

Eddy current measurements on samples with high conductivity, namely metal, are easier to perform than measurements on samples of low conductivity, since the generated magnetic field scales with the sample conductivity. In a first step we tested our eddy current magnetometer on metal samples, e.g. a cm-sized piece of Titanium of 1 mm thickness. In **Error! Reference source not found.** we show the amplitude of the secondary magnetic field (i.e. the magnetic field from the induced eddy currents) in units of the primary magnetic field (top). Increasing the frequency of the rf field, the secondary amplitude increases until the skin depth reaches the thickness of the sample. This comes together with a change in phase shift of the secondary magnetic field (bottom). In simple terms this can be understood as transitioning from a $-\frac{\pi}{2}$ phase shift as expected from Faraday's law of induction to a π phase shift as expected for a reflection. The details will be subject to further investigation.
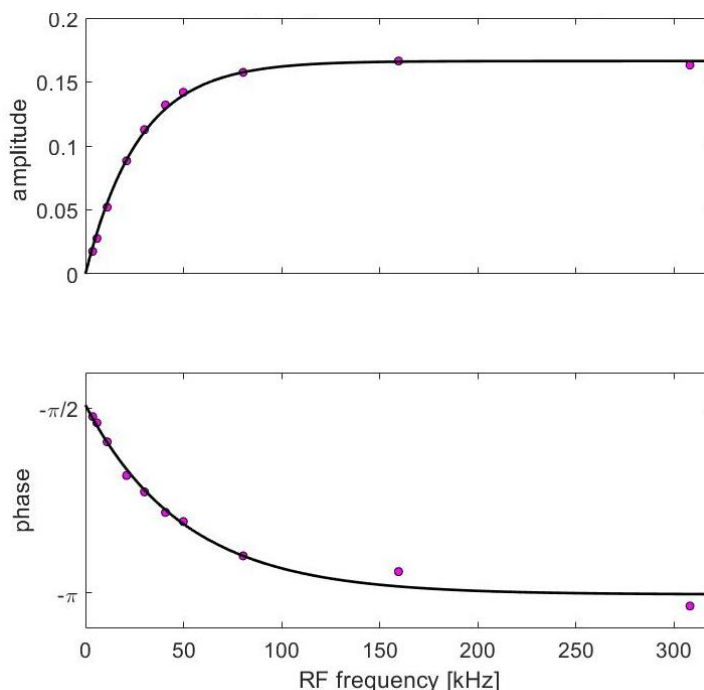

Figure 12. Amplitude (top) and phase (bottom) of the secondary magnetic field induced in a 1 mm thick Titanium piece.

4.3 Saltwater measurement

First, we characterize the magnetometer without any conductive object by applying an oscillating magnetic field in the $\hat{y}$ direction. Figure 13 (a) shows the Lorentzian and dispersive responses in the X and Y quadrature around the Larmor frequency of 1978 kHz. The secondary peaks are due to neighbouring Zeeman levels that are resolved to the nonlinear Zeeman effect. Keeping the oscillating field on resonance we observe the data points labelled B_1 in Figure 13 (b) with significant amount of noise in the Y output. The noise is mainly due to temporal fluctuations of the magnetic bias field and corresponds to a relative change of about 10^{-6}. This small number illustrates the need for a very stable bias magnetic field to precisely measure an oscillating magnetic field.

In the case of our saltwater sample the thickness of the sample is much smaller than the skin depth, and the secondary field is 90° out of phase with the primary field. For a setup with a single excitation coil the ratio of secondary to primary field is $\alpha = B_{ec}/B_1 \approx 1.5 \cdot 10^{-4}$ (using a $(2cm)^3$ container of saltwater with conductivity 10 S/m and Larmor frequency 2MHz). From the measurement described above the smallest detectable field ratio is only of the order $\alpha_{min} = B_{ec}/B_1 \approx 10^{-2}$. This is clearly not sufficient to detect low conductivity objects like saltwater.

Increasing the primary field amplitude leads to a stronger secondary field. However, as can be seen from the Lorentzian response function above, if the primary field $B_1 \geq B_{sat} = 2\delta\omega/\gamma$, the response will power-broaden, leading to signal reduction and nonlinearity. Furthermore, if the dominating noise is proportional to both primary and secondary field (e.g. magnetic bias field fluctuations), increasing the primary field will not yield an advantage.

We have developed a differential technique that allows to detect small changes in the eddy current signal enabling to detect low-conductivity samples.
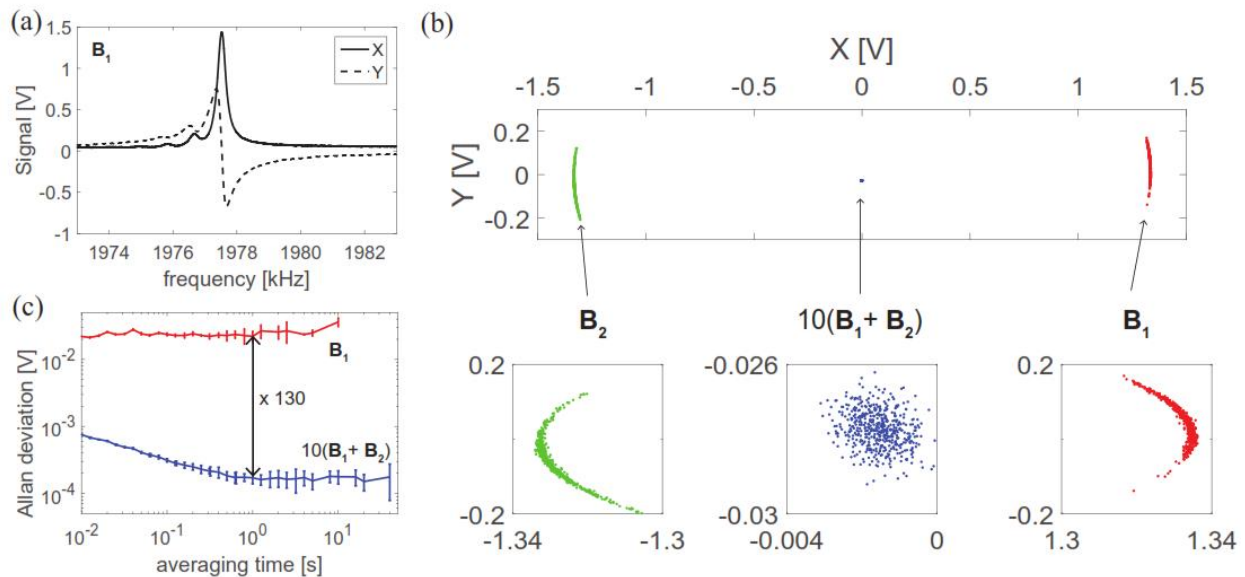

Figure 13. (a) Lock-in outputs X and Y as a function of the frequency of the oscillating magnetic field B_1 (b) Lock-in outputs when $\omega = \omega_L$. Each data point was integrated for 40 ms. Three data sets each with 500 points are shown: one where B_1 was applied, one where B_2 was applied and one where $10 (B_1 + B_2)$ was applied (c) Allan deviation of the Y -output when B_1 was applied (top trace) and when $10 (B_1 + B_2)$ was applied (bottom trace). Figure and caption from [Jensen19].

We use a second coil (denoted coil 2 in the setup figure) that generates a magnetic field B_2 such that in the absence of a conductive object, the field $B_1 + B_2 \approx 0$ is cancelled at the position of the vapor cell. Coil 2 is placed further away from the conductive object, such that the induced eddy currents are mainly

from coil 1 only. With this technique we can mitigate the above-mentioned problems and demonstrate a dramatic improvement to $\alpha \approx 10^{-4}$ for our measurements on saltwater.

This is shown in Figure 13 (b) where the three datasets only coil 1 (red), only coil 2 (green) and differential technique with 10 times higher amplitude (blue) clearly show the reduction in noise. The improvement can also be observed in the Allan deviation in plotted in Figure 13 (c).

We continue with measurements of saltwater with conductivities varying from 3.8 S/m to 24.1 S/m where we scan the container over a length of 50 mm a few mm above coil 1. As shown in **Error! Reference source not found.** we clearly observe a change in the Y quadrature when the container is on top of coil 1. The X outputs (not shown) stay at zero within their statistical uncertainties. For the measurement shown in the figure we scan the container 20 times and plot the relative difference of the signal in units of the primary field. We fit a Gaussian function to guide the eye and to extract the maximum in the change of signal.

We emphasize that we detect the saltwater with good signal to noise ratio (SNR). For the averaged traces we have the SNR of 6.4, 20, and 46 for the conductivities 3.8, 10.7 and 24.1 S/m. This demonstrates that our setup should be able to measure conductivities below 1 S/m with a SNR > 1 and that it should be possible to detect and image biological tissue which has $\sigma \leq 1$ S/m with our optical magnetometer.
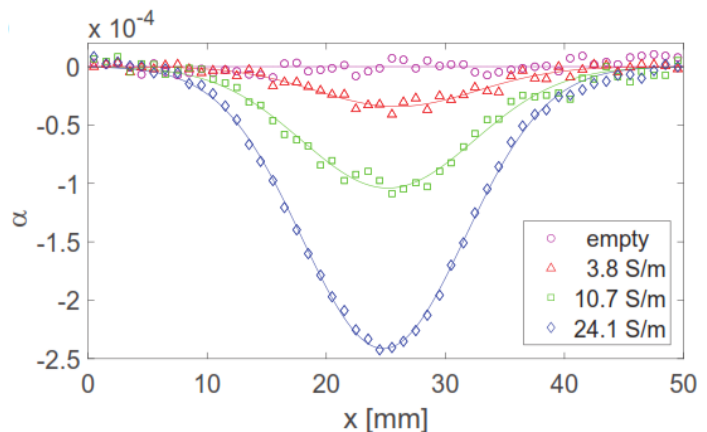

Figure 14. Detection of salt-water. Relative change in signal using about 20 averages. Data are binned according to their position with one binned data point per 1 mm. Figure from [Jensen19].

We investigate the dependence of the induced field to primary field ratio with the conductivity. As shown in Figure 15 (a) it is proportional to the conductivity which agrees with the estimate $\alpha \approx -A\,\sigma\omega\mu_0$ where A is a geometrical factor and μ_0 is the vacuum permeability [Jensen19]. This estimate also predicts a linear scaling with the Larmor frequency which is experimentally validated as shown in Figure 15 (b). The size of signal increases with the amplitude of the primary field. The dependency starts out linearly before saturation occurs for higher amplitudes (see Figure 15 c). This saturation is not expected when using the differential technique. We note that when only B_1 is applied, the saturation happens at 10 times lower amplitudes. To avoid saturation effects, all measurements have been taken below the respective saturation level.
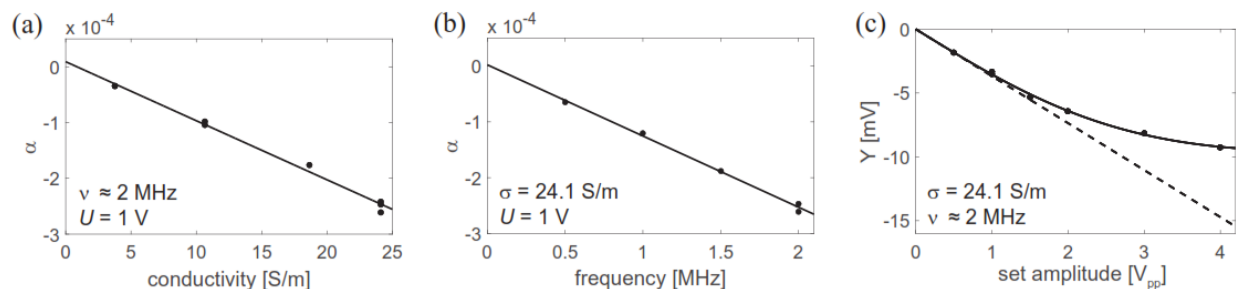

Figure 15. (a)–(b) Relative change in signal as a function of conductivity and applied frequency. Data are shown together with linear fits. (c) Change in signal in mV as a function of the set amplitude U on the function generator connected to the two coils. Data are shown together with a fit to the function $cU/(1 + [U/U_{sat}]^2)$ (solid line) and the linear part of the fit function $c\,U$ (dashed line). A 1 V set amplitude corresponds to the fields $10B_1 = -10B_2 = 45$ nT peak-to-peak amplitude. Figure and caption from [Jensen19].

5   Strong field OPM

5.1   Magnetometer Probe Prototype

The caesium D2 line, is composed of six hyperfine transitions at zero magnetic field. They are distributed in two groups of three lines close to each other, so they appear as two dips, in the figure below. When exposed to a strong magnetic field, they split into 16 lines - eight strong and eight weak - as seen in the following spectrum. The eight weak lines are located around up to +/- 30 GHz and are barely visible.
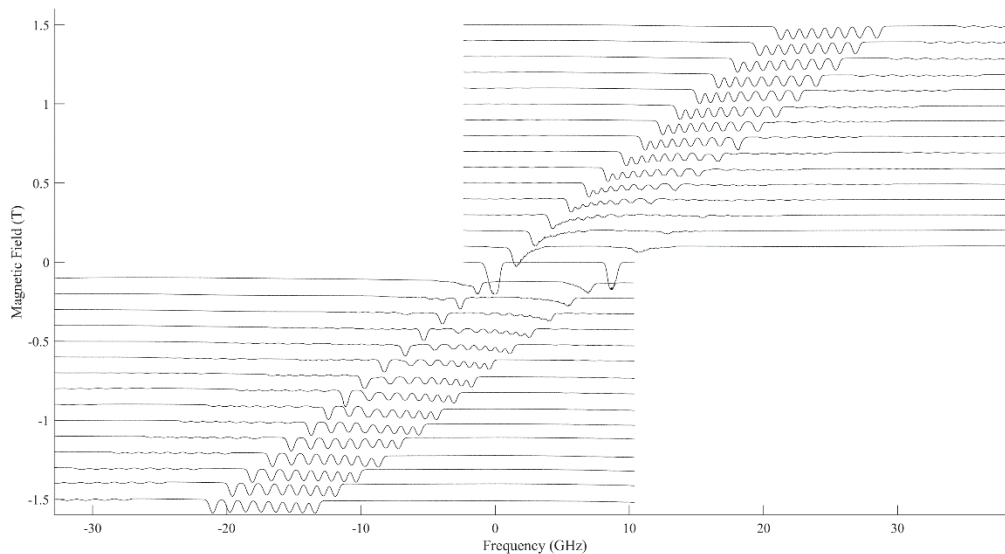

Figure 16. Absorption lines for different magnetic field strengths.

The leftmost of the eight strong lines in the above spectra is seen to shift linearly with the magnetic field strength. This is the transition from the ground state with maximum total and projected angular momentum, to the excited state with maximum total and projected angular momentum.

Investigating to a very high accuracy, the line shift also has a tiny quadratic contribution, such that the shift is given by the equation

$\Delta\nu = \gamma_1 B + \gamma_2 B^2$.

The value of γ_1 is currently known as 13.992 5(63) GHz/T. The value of γ_2 has never been reported in the literature, but theory estimates it to be about 0.44 MHz/T^2.

To accurately measure the frequency shift, we have a reference sensor placed in a magnetic shield at zero field, and a probe inside the magnetic field of the MRI scanner. The reference is configured with linearly polarized light, such that a small residual field inside the magnetic shield doesn't shift the line, but only broadens it a little. Using electrooptical modulation we can make laser frequency sidebands, such that transitions at zero and high field are probed simultaneously. This way the frequency shift can be measured, and hence the magnetic field determined.

Figure 17 is a schematic of the optics inside the strong field OPM sensor head. On-resonant laser light enters through the single-mode fibre (blue). The light passes through the cell, is retroreflected and directed out of the sensor head through the multi-mode fibre (orange). The heating laser is delivered through the yellow multimode fibre and heats up an optical filter in thermal contact with the caesium cell.
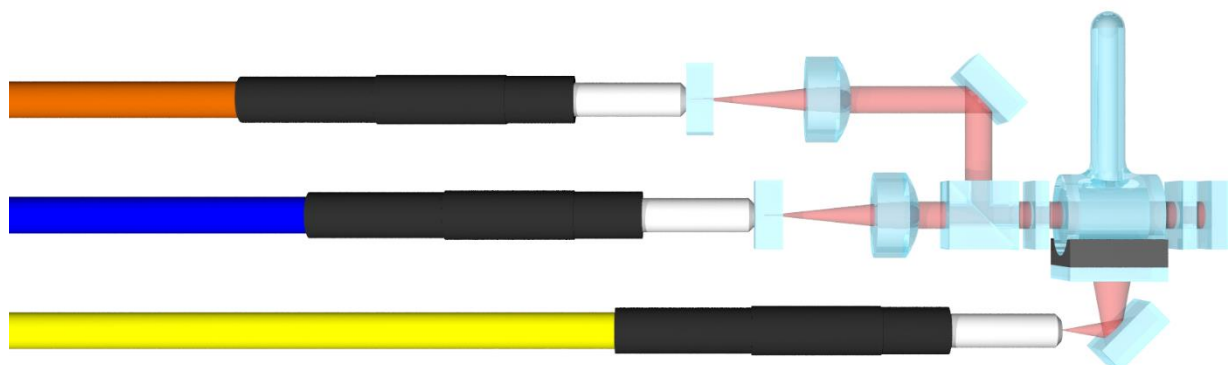
Figure 17. Strong field OPM sensor head optics schematic.

One reference sensor head and four probe sensor heads have been made. They enable performing saturated absorption spectroscopy in a completely metal-free assembly. The three main challenges solved are:

- *Coupling light into the output multimode fiber with a high efficiency.* Better than 90 % is achieved, and the fiber coupling is stable during daily handling and use.
- *Removing cavity fringes from the fibers.* This is achieved by placing the end faces of the input and output fibers up against AR coated windows, with index matching gel at the interface. As seen in the following figure, the fringes are nicely suppressed.
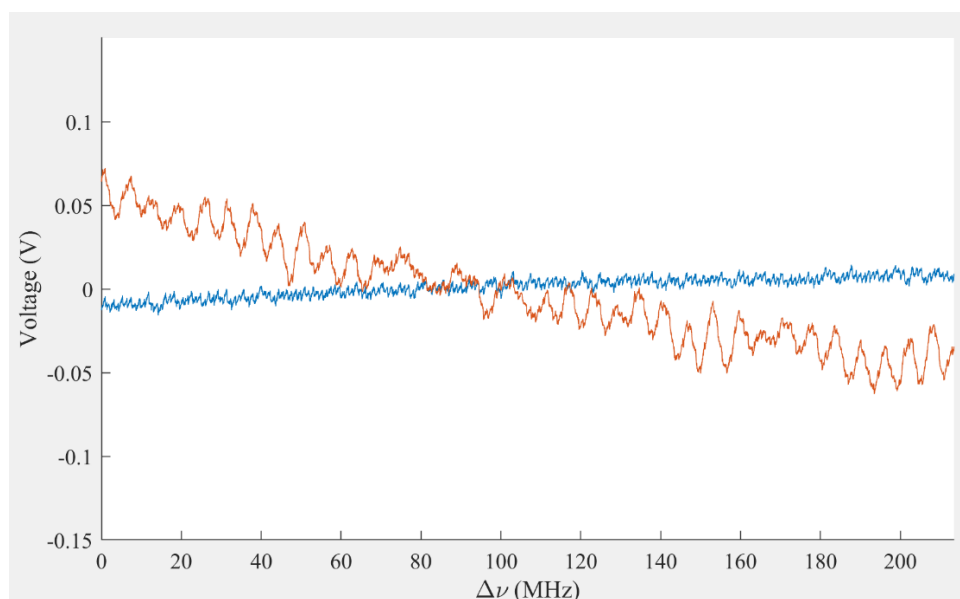

Figure 18. Signal with (red trace) and without (blue trace) fringes when scanning laser frequency.

- *Implementing optical heating.* The atomic density in the vapor cell can now be increased by about a factor 10. This significantly increases the signal strength.

The probes are made with an HP Multi Jet Fusion 3D printer, as seen in the following photos.
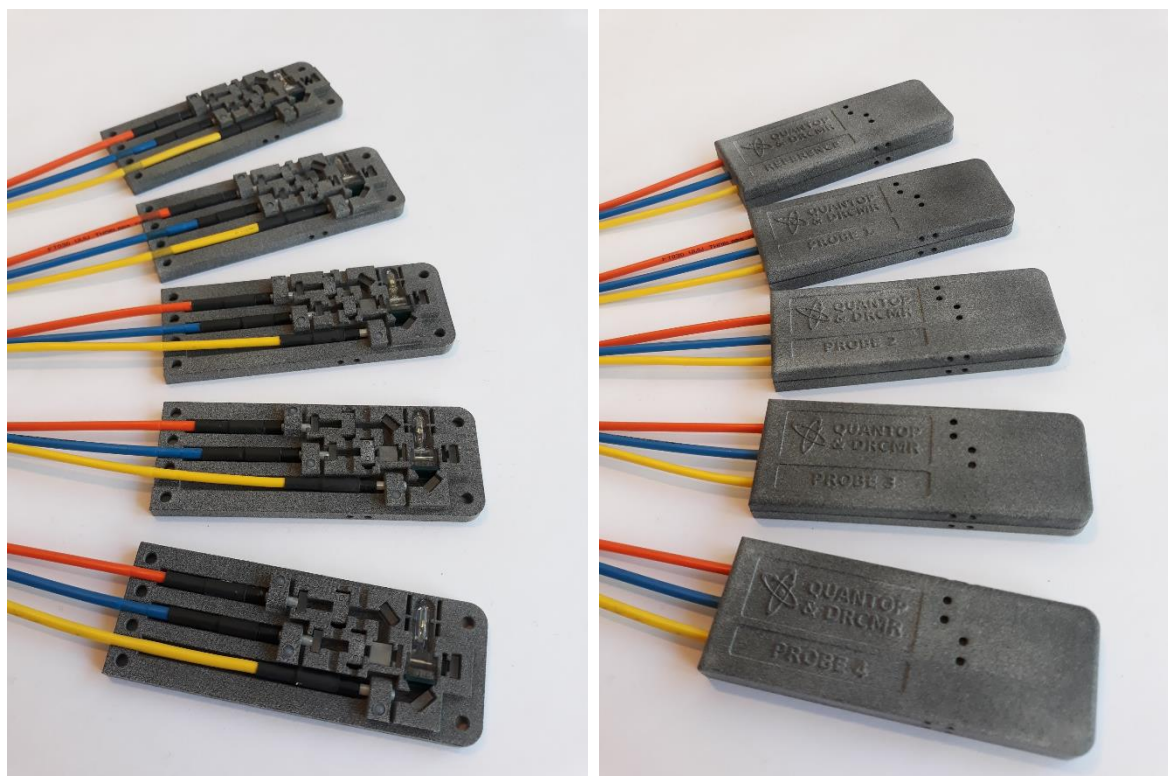
Figure 19. Photograph of the assembled OPM sensors, open (left) and closed (right).

5.2   Absolute calibration of magnetometer

In order to realize highly accurate magnetometry at strong magnetic fields with caesium we are currently working to measure the constants γ_1 and γ_2 with high precision. Our preliminary estimates are:

- γ_1 = 13.994323(29) GHz/T
- γ_2 = 0.4707(14) MHz/T^2

This can be done by reconfiguring the magnetometer setup slightly and comparing to a proton spectroscopy reference, using the hardware of the MRI scanner. The high accuracy of the proton gyromagnetic ratio allows for a very accurate determination of the magnetic field, which is necessary for the calibration. A sphere of ultrapure water is used as a proton reference:

A proper determination of the sensitivity has not been performed yet. It is expected that the analogue feedback that keeps the laser sideband resonant with the optical transition during field changes, adds significant amounts of noise, which could be removed by implementing a digital feedback. For this reason, we aim to perform a sensitivity measurement with the *feedback on*, and hence full range of the magnetometer, and a measurement with the *feedback off*, and hence very low magnetometer range, but with increased sensitivity. The increased sensitivity should then also be possible to realize with the full magnetometer range, using a digital feedback.

Figure 20. Sphere of ultrapure water used for proton reference.

macQsimal	Title	Deliverable Number
	Low-density OPM demonstrator and	**D4.5**
Project Number	**benchmarking report**	Version
820393		**1**

5.3 19-Inch Rack Integration

Figure 21. Complete optical and electronic equipment in the vicinity of the MRI scanner.

Steps are being made to integrate all the hardware in a 19-inch rack, to make daily operation in a hospital setting easy and safe. For stability of the system, the goal is to have an all-fibre-coupled setup using 19-inch modules like the one shown here:
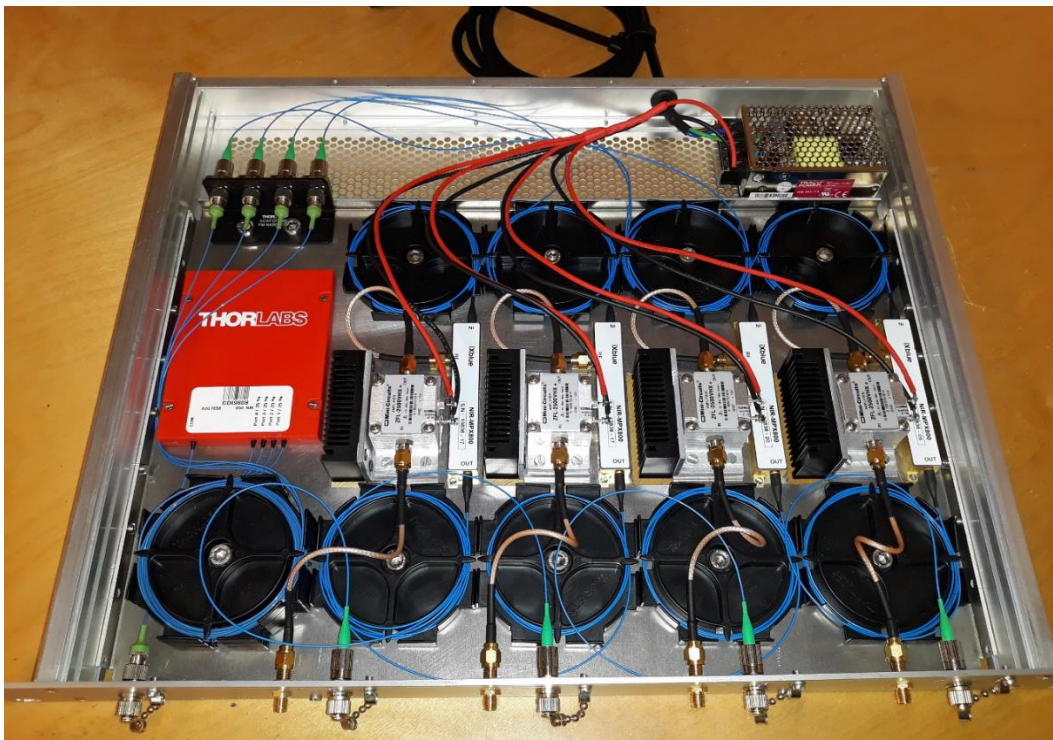

Figure 22. Fibre optics module distributing laser light with modulation to all OPM sensors.

5.4 Proof-of-Concept results

We have made proof-of-concept measurements of two MRI sequences. A spiral sequence and an echo-planar sequence:
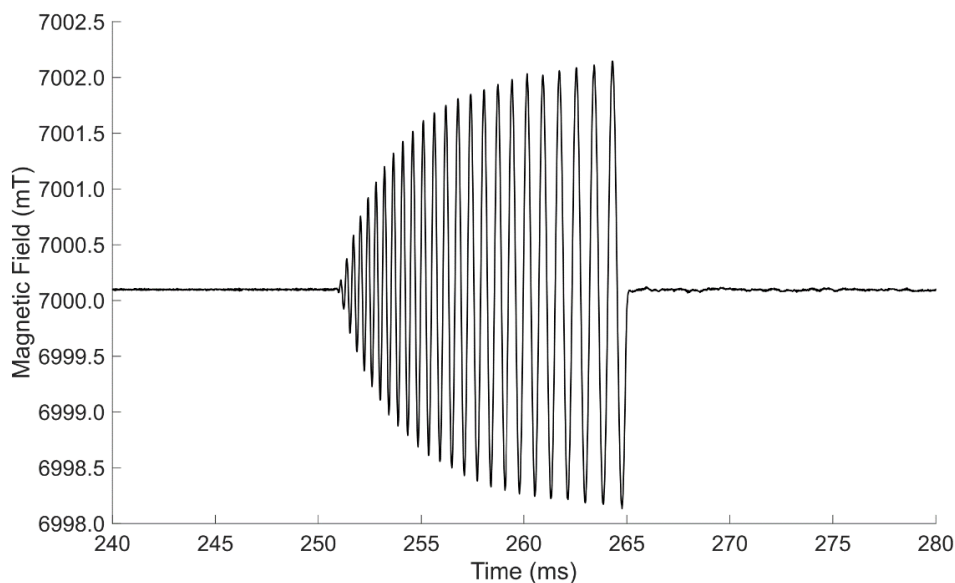

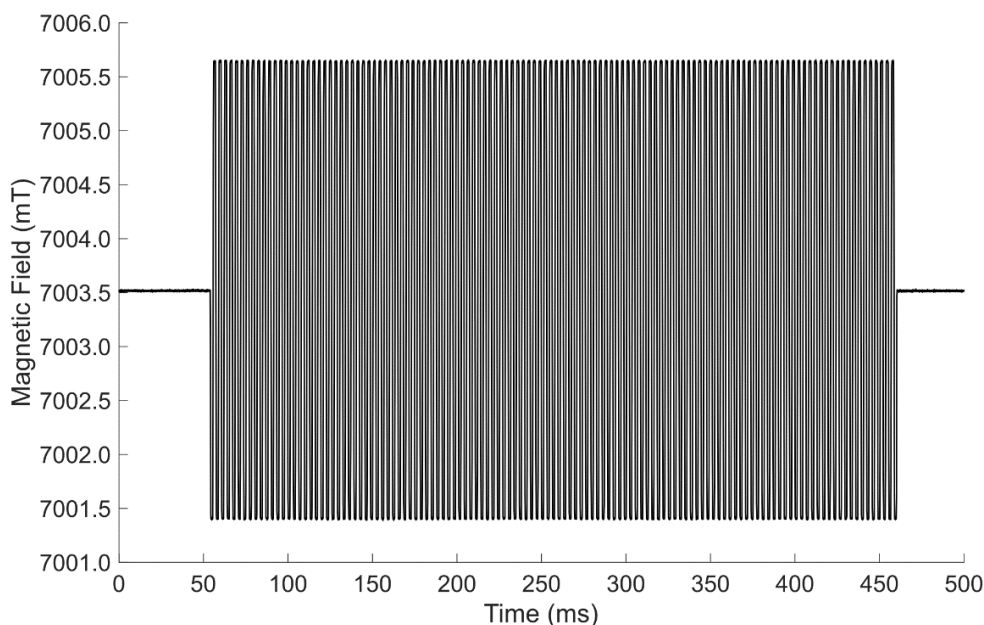*Figure 23. Magnetic field during a spiral sequence.*

Figure 24. Magnetic field during an echo-planar sequence.

It has become clear that what might be an advantage of our system compared to NMR field probes, is not just that our probe is non-metallic, but also that it works continuously, instead of pulsed.

To say what is signal and what is noise in these measurements we need to do a series of other experiments. This includes using more probes, turning feedback both on and off, and measuring both MRI sequences and no sequences. Once we have determined the calibration constants γ_1 and γ_2, this will be our focus.

6   Conclusion

We have demonstrated low-density OPMs using glass-blown vapour cells. We have tested and characterized vapour cells with caesium and paraffin anti-relaxation coating for the use in the low field OPM demonstrator. Commercial vapour cells filled only with caesium have been tested for the use in a strong field OPM.

Using off-resonant Faraday interaction we have tested and benchmarked a fibre-coupled OPM sensor with 200fT/sqrt(Hz) sensitivity at low magnetic fields (75 fT/sqrt(Hz) for rf magnetic field sensing). This sensor would allow to repeat MCG measurements that have been previously demonstrated with a similar free-space setup. We have developed techniques for imaging of electrical conductivities that allowed the first contact-less measurement of few mL volumes of near-Siemens-per-meter conductivity salt-water phantoms.

Furthermore, using on-resonant Doppler-free absorption, we have developed an array of OPMs suitable for measurements of strong magnetic fields within an MRI scanner and demonstrated its capability by measurement of the diamagnetic shift of caesium with unprecedented precision.

7   References

[Jensen19]   Jensen, K., Zugenmaier, M., Arnbak, J. *et al.* Detection of low-conductivity objects using eddy current measurements with an optical magnetometer. *Phys Rev Research* **1**, 033087 (2019).

[Jensen18]   Jensen, K., Skarsfeldt, M.A., Stærkind, H. *et al.* Magnetocardiography on an isolated animal heart with a room-temperature optically pumped magnetometer. *Sci Rep* **8**, 16218 (2018).

[Julsgaard03]   Julsgaard, B., Sherson, J., Sørensen, J. L. and Polzik, E. S. Characterizing the spin state of an atomic ensemble using the magneto-optical resonance method, *J. Opt. B: Quantum Semiclass. Opt.* **6** 5 (2003).